JACS
JOURNAL OF THE AMERICAN CHEMICAL SOCIETY
pubs.acs.org/JACS

Article

Defect Tolerance via External Passivation in the Photocatalyst $SrTiO_3$:Al

Kanta Ogawa,* Seán R Kavanagh, Fumiyasu Oba, and Aron Walsh

Cite This: https://doi.org/10.1021/jacs.5c07104

Read Online

ACCESS | Metrics & More | Article Recommendations | Supporting Information

ABSTRACT: The efficiency of solar-to-energy conversion in semiconductors is limited by charge carrier recombination, often via defect-induced gap states. Although some materials exhibit an intrinsic defect tolerance that avoids fast recombination channels, there are few examples among metal oxides. We investigate the water splitting photocatalyst $SrTiO_3$, where photocatalytic performance is enhanced by extrinsic Al doping. We propose that defect tolerance emerges through a passivation effect that effectively eliminates in-gap states and nonradiative recombination. First-principles defect calculations show that oxygen vacancies are the primary defect species in $SrTiO_3$ under oxygen-poor synthetic conditions, which provide in-gap states that are active for carrier capture. Al substitutions are preferred at Ti sites adjacent to the oxygen vacancy, forming $[V_O\text{-}Al_{Ti}]$ defect complexes. As the oxygen vacancy in-gap state is derived from Ti 3d−Ti 3d interactions across the vacancy, substituting Ti with Al deactivates this interaction and eliminates the in-gap state. The absence of valence d orbitals in Al is key for in-gap state reduction, as supported by the consideration of other dopants such as Sc. Our study illustrates how an orbital-wise understanding of defect states can enable doping strategies to achieve defect tolerance in materials like $SrTiO_3$, paving the way for improved solar-to-energy conversion.

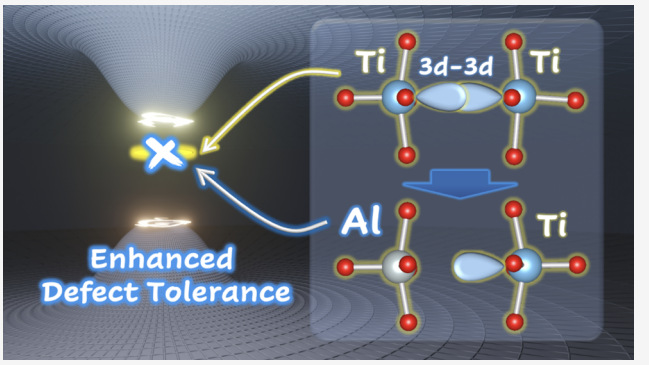

INTRODUCTION

Strontium titanate ($SrTiO_3$) has long been a prototype water splitting photocatalyst for clean H_2 production.[1−3] Various attempts have been made to enhance catalytic activity, including doping,[4−6] morphology tuning,[7−9] and surface modification.[10−13] The most striking enhancement was achieved with Al doping and appropriate surface modifications, yielding more than 90% quantum efficiency for water-splitting under ultraviolet irradiation.[14,15] Here, most of the photoexcited carriers are not annihilated by carrier recombination but split water into H_2 and O_2 without external electric fields.[15] This success opened a new chapter toward practical water splitting photocatalysis.[16]

The proposed role of Al doping is to reduce the density of in-gap trap states, believed to be Ti^{3+} states. These trap states provide recombination channels for photogenerated carriers,[6] as supported by X-ray photoelectron spectroscopy and electronic structure theory.[17] This is in contrast to the typical role of extrinsic doping in semiconductors, which often generates dopant states and/or charge carriers.[18−22] The role of Al^{3+} has been linked to its lower valency than the host B-site Ti^{4+}, given the photocatalytic activity of $SrTiO_3$ can be also improved by other lower oxidation state dopants such as Ga^{3+} and Mg^{2+} but deteriorated by Ta^{5+}.[6,23] However, the mechanistic origin, including how the Ti^{3+} trap state is suppressed by Al doping, and the link to lower valency, remains unresolved.

In this study, we find that the defect tolerance enabled by Al doping of $SrTiO_3$ emerges as a passivation effect. Following a first-principles assessment of the intrinsic defect chemistry of $SrTiO_3$, we discuss the origins of defect trap states based on their orbital interactions. The dominant deep trap is the Ti^{3+} state derived from the oxygen vacancy. This state is passivated by Al doping through the formation of a $[V_O\text{-}Al_{Ti}]$ complex, which deactivates the orbital interactions between adjacent Ti-3d states. The absence of valence d orbitals, rather than the lower valency of Al, is found to be key to this behavior.

The distinctive role of Al doping in $SrTiO_3$ highlights that defect tolerance can be engineered. Defect tolerance, linked to the avoidance of deep trap states[24] or nonradiative recombination channels,[25,26] is usually linked to the fundamental properties of the host crystal, such as an antibonding-type upper valence band[27−32] or bonding-type

Received: April 28, 2025
Revised: June 5, 2025
Accepted: June 5, 2025

lower conduction band.[31−34] $SrTiO_3$ is not "intrinsically" defect tolerant from this viewpoint. Rather, wide-gap semiconductors like $SrTiO_3$, with a band gap larger than 1.6 eV, have been less successful due to inherent high (low) ionization potential (electron affinity) and/or high ionicity.[35] The present study demonstrates the potential for defect-state engineering via doping to passivate intrinsic in-gap defect states and suppress carrier recombination.

RESULTS AND DISCUSSION

Electronic Structure of $SrTiO_3$. Cubic $SrTiO_3$ has a typical ABX_3 perovskite crystal structure with Sr on the cuboctahedral A-site and Ti on the octahedral B-site (Figure 1a). The electronic structure of pristine $SrTiO_3$ was calculated

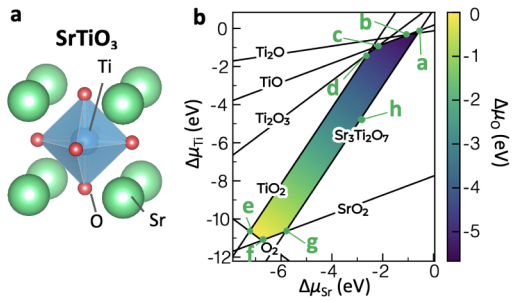

Figure 1. (a) Crystal structure of the cubic perovskite phase of $SrTiO_3$. (b) Sr−Ti−O ternary chemical potential diagram showing the stable region of $SrTiO_3$ due to the limits imposed by competing phases.

using the Heyd−Scuseria−Ernzerhof (HSE06) hybrid exchange-correlation functional[36] (Table S1). The calculated direct (3.72 eV) and indirect (3.34 eV) band gaps are in reasonable agreement with experimental values (3.75 and 3.25 eV, respectively).[37] Bonding and antibonding interaction between Ti and O give rise to the valence and conduction bands respectively, while the orbital interactions at the valence band maxima (VBM) and conduction band minima (CBM) are primarily nonbonding (Figure S1).[38] This electronic structure does not imply intrinsic defect tolerance, although the nonbonding band edges may be less harmful than the bonding VBM and antibonding CBM for avoiding deep traps.

The phase stability of $SrTiO_3$ was determined by calculating the total energy of the competing phases within the Sr−Ti−O chemical space using doped package[39] (Table S2). All possible competing phases (stable and metastable ones within a tolerance of 0.1 eV/atom) were obtained from the Materials Project[40] database and their energies were computed using the HSE06 hybrid functional, in order to determine the stable region of the elemental chemical potentials ($\Delta\mu_{Sr}$, $\Delta\mu_{Ti}$, $\Delta\mu_O$), where each $\Delta\mu_i$ represents the chemical potential relative to the standard chemical potential (i.e., μ_{Sr}°, μ_{Ti}°, $\mu_O^\circ = 1/2\,\mu_{O_2}^\circ$, respectively). The sum of $\Delta\mu_{Sr}$, $\Delta\mu_{Ti}$, and $\Delta\mu_O$ is given by the formation energy of $SrTiO_3$, ΔE_f ($SrTiO_3$), namely,

$$\Delta\mu_{Sr} + \Delta\mu_{Ti} + 3\Delta\mu_O = \Delta E_f(SrTiO_3)$$

In addition, $\Delta\mu_{Sr}$, $\Delta\mu_{Ti}$, $\Delta\mu_O$ should not stabilize other competing phases such as TiO_2, namely,

$$\Delta\mu_{Ti} + 2\Delta\mu_O \le \Delta E_f(TiO_2)$$

Such constraints determine the chemical potential ranges for $\Delta\mu_{Sr}$, $\Delta\mu_{Ti}$, $\Delta\mu_O$ that stabilize $SrTiO_3$, as represented by the colored area in Figure 1b defined by the seven limit conditions (**a**−**g**). Here, we see that $SrTiO_3$ occupies quite a wide range of chemical potentials in the Sr−Ti−O chemical space, with $\Delta\mu_{Sr}$ and $\Delta\mu_O$ varying by ∼6 eV and $\Delta\mu_{Ti}$ varying by ∼10 eV within the stable region of $SrTiO_3$.

Defect Formation Energy and Concentration. Within the supercell formalism for computing defect energetics, the formation energy of a defect X in charge state q, $E^f_{X,q}(\varepsilon_F, \mu)$, is given as[41−43]

$$E^f_{X,q}(\varepsilon_F, \mu) = E_{X,q} - [E_H + \sum_i n_i\mu_i + q\cdot(-\varepsilon_F)] + E_{corr}(q) \quad (1)$$

Here, $E_{X,q}$ is the total energy of the supercell containing the defect, while E_H is the energy of the corresponding pristine bulk supercell. $\sum_i n_i\mu_i$ represents the energy of n_i atom of kind i from a reservoir with chemical potential μ_i. Analogously, $-q\varepsilon_F$ accounts for the energy of charge q from the reservoir having the given chemical potential of electrons, i.e., the Fermi level ε_F. The last term $E_{corr}(q)$ is the charge-state dependent correction to account for spurious electrostatic interactions arising from the finite supercell size. The extended Freysoldt−Neugebauer−Van de Walle (eFNV) correction scheme was employed in the present study.[44,45]

While μ_i and ε_F are variable, $E_{X,q}$, E_H should be calculated carefully for an accurate determination of the defect formation energy. Herein, the HSE06 hybrid functional was employed. In addition, $E_{X,q}$ depends on the calculated (relaxed) defect structure, which is sensitive to the choice of initial geometry.[46] The standard approach, based on local optimization of a defect-containing supercell, sometimes misses the true ground state by falling into a local minimum.[47] To avoid this, we employed a robust yet efficient searching method, where the initial structures are generated through chemically guided bond distortions and rattling (the ShakeNBreak approach).[48,49] Effective sampling of the potential energy surface enables us to identify energy-lowering structural reconstructions.

By calculating the formation energy of all the possible native defects including vacancies, antisites, and interstitials (Table S3), a defect formation energy diagram at a certain chemical potential condition is obtained (e.g., Figure 2b for the oxygen poor limit). From this diagram, we can estimate the concentration of defect X in charge state q ($C_{X,q}$) at a certain temperature T. Since $C_{X,q}$, as well as the concentrations of free holes and electrons (p and n), depend on ε_F , the charge neutrality condition self-consistently determine ε_F , and thus $C_{X,q}$, p, and n (see the Experimental Section for details).[50,51]

Figure 2a shows the carrier concentration in undoped $SrTiO_3$ as a function of anneal temperature and chemical potential during the synthesis process. The frozen defect approximation is applied to mimic a synthetic condition where the material is annealed under elevated temperatures and cooled rapidly to room temperature.[51,52] Defects are formed at the elevated annealing temperature but remain during cooling due to the assumed large kinetic barriers for diffusion and annihilation. The temperature dependence of the band gap[53] (at annealing temperatures) was also taken into account. Clearly, n-type conditions (orange) dominate over p-type ones (blue). Higher electron densities are achievable compared to hole densities, showing the native n-type preference of

https://doi.org/10.1021/jacs.5c07104
J. Am. Chem. Soc. XXXX, XXX, XXX−XXX

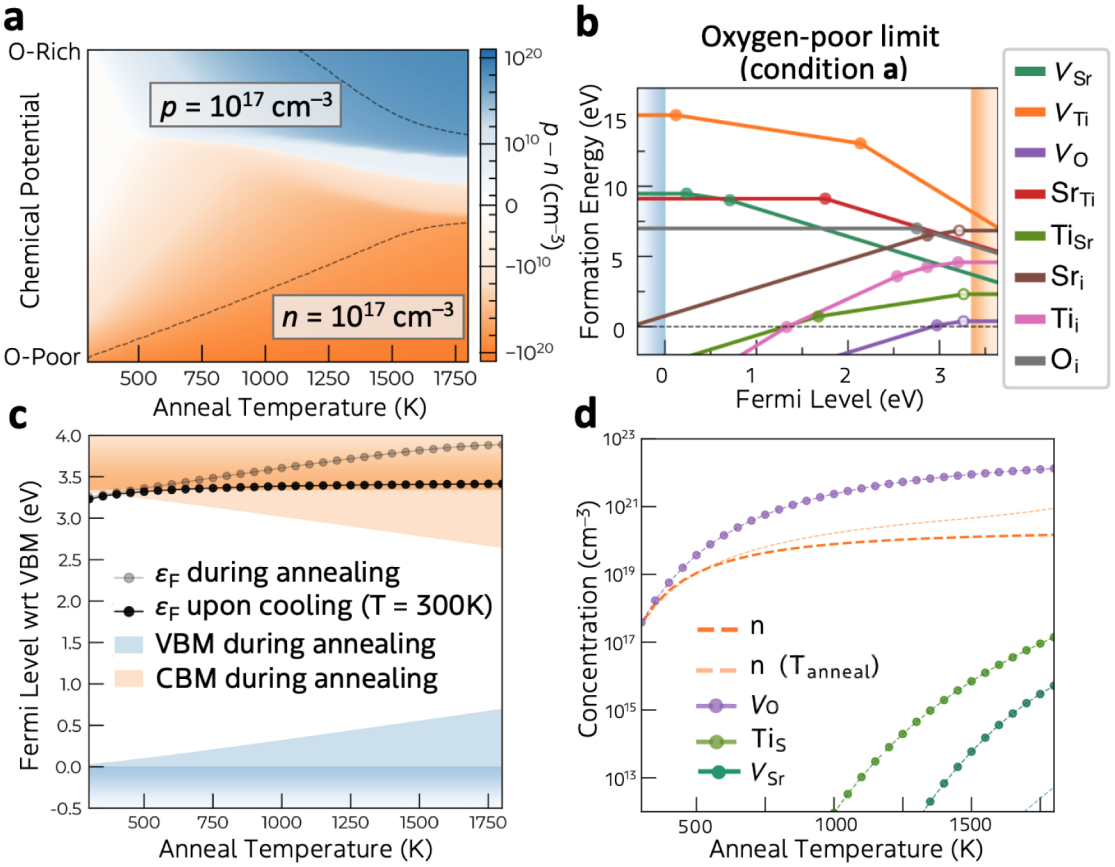

Figure 2. (a) Calculated carrier concentration in undoped $SrTiO_3$ at room temperature, as a function of annealing temperature and chemical potential conditions. Contour lines correspond to the carrier concentration of 10^{17} cm^{-3}. (b) Formation energies and transition levels (filled circles) of native defects in $SrTiO_3$ at the oxygen-poor limit (condition a: $\Delta\mu_O = -5.67$, $\Delta\mu_{Sr} = -0.62$, $\Delta\mu_{Ti} = -0.25$ eV), where shallow donor levels associated with electronic states inheriting host band edge orbital characteristics are designated by open circles. (c) Calculated self-consistent Fermi level positions in undoped $SrTiO_3$ during annealing (gray) and upon cooling to room temperature (300 K; black), assuming the oxygen-poor limit. (d) Room temperature carrier and defect concentrations as a function of annealing temperature, assuming the oxygen-poor limit.

undoped $SrTiO_3$. Although p-type conductivity is observed for undoped-$SrTiO_3$ at high temperature and under high oxygen partial pressure,[54] consistent with the calculated carrier polarity, the p-type regime is limited because of the quenched-in oxygen vacancy population even at a low temperature.[55] Note that the highly active $SrTiO_3$:Al photocatalyst is synthesized using a flux-assisted method, where the crystal grows in the molten salt of $SrCl_2$ at 1423 K.[14,15] In this growth condition, the oxygen chemical potential should be poor due to the lack of contact with O_2 molecules in air and a high temperature. Indeed, $SrTiO_3$:Al exhibits n-type character with an estimated electron concentration (n) of 1.7×10^{17} cm^{-3} from its Mott−Schottky plot.[56] Therefore, we mainly focus on oxygen-poor conditions hereafter.

The defect formation energy diagram at the oxygen-poor limit (condition **a** in Figure 1b) is shown in Figure 2b. The formation energies at other chemical potential limits are described in Figures S2 and S3. Under the oxygen-poor limit condition (condition **a**: $\Delta\mu_O = -5.67$, $\Delta\mu_{Sr} = -0.62$, $\Delta\mu_{Ti} = -0.25$ eV) considered in Figure 2c, $SrTiO_3$ presents an n-type character with ε_F near the CBM. Figure 2d shows the defect concentration plotted versus the annealing temperature at the oxygen poor limit. Oxygen vacancy (V_O) is the highest concentration defect species, followed by titanium-on-strontium antisite (Ti_{Sr}). The latter is suppressed under Sr-rich condition (Figure S4).

As established from experiment,[17,57] the oxygen vacancy concentrations in $SrTiO_3$ under O-poor conditions and at high annealing temperatures are extremely high (>10^{21} cm^{-3}; Figure 2d), approaching percent-level concentrations relative to the oxygen sites (having a bulk site concentration of $\sim 5 \times 10^{22}$ cm^{-3}). At these high concentrations, there is likely to be non-negligible V_O−V_O interactions,[58] implying that the predicted defect concentrations should be treated semiquantitatively. Still, such effects would not alter the conclusion that the oxygen vacancies are the dominant defect species under O-poor conditions.

Nature of the V_O Deep State. As expected, oxygen vacancies (V_O) have the lowest formation energy in the oxygen-poor region, with the dominant charge state depending on ε_F (Figures 2b and S5). The ε_F position where the defect formation energies for different charge states (q_1 and q_2) are equal is called a charge transition level $\varepsilon(q_1/q_2)$. These are also known as carrier trap levels because they define the thermal ionization energies or electron affinities of the donor/acceptor. The charge transition of V_O from +2 to +1, i.e., $\varepsilon(+2/+1)$, occurs at 0.37 eV, and from +1 to 0 at 0.08 eV below the CBM (Table S5). The former means that 0.37 eV is required to thermally excite one electron from V_O^{+1} to form V_O^{+2}, defining the trap energy of an electron at V_O^{+2} (Figure S5). The present result suggests that the oxygen vacancy is a double donor where one electron is easily released to the conduction band

https://doi.org/10.1021/jacs.5c07104
J. Am. Chem. Soc. XXXX, XXX, XXX−XXX

while the second tends to be trapped within the band gap, consistent with the previous experiment[59,60] and calculation results.[61−64] The calculated transition levels are in good agreement with those estimated by analyzing the temperature-dependent transport behavior, where ionization energies of 0.3 eV for $\varepsilon(+2/+1)$ and <3 meV for $\varepsilon(+1/0)$ were reported.[65]

These charge transition levels reflect the underlying difference in the single-particle electronic bands. As shown in Figure 3, while the closed-shell V_O^{+2} does not induce an in-gap state, V_O^{+1} produces a localized state below the CBM, which causes the in-gap transition level in Figures 2b and S5. In this study, we show that Al doping to $SrTiO_3$ reduces trap states. Before investigating the effect of Al doping, we examine the origin of trap states at oxygen vacancies by analyzing the single-particle electronic DOS for each V_O charge state.

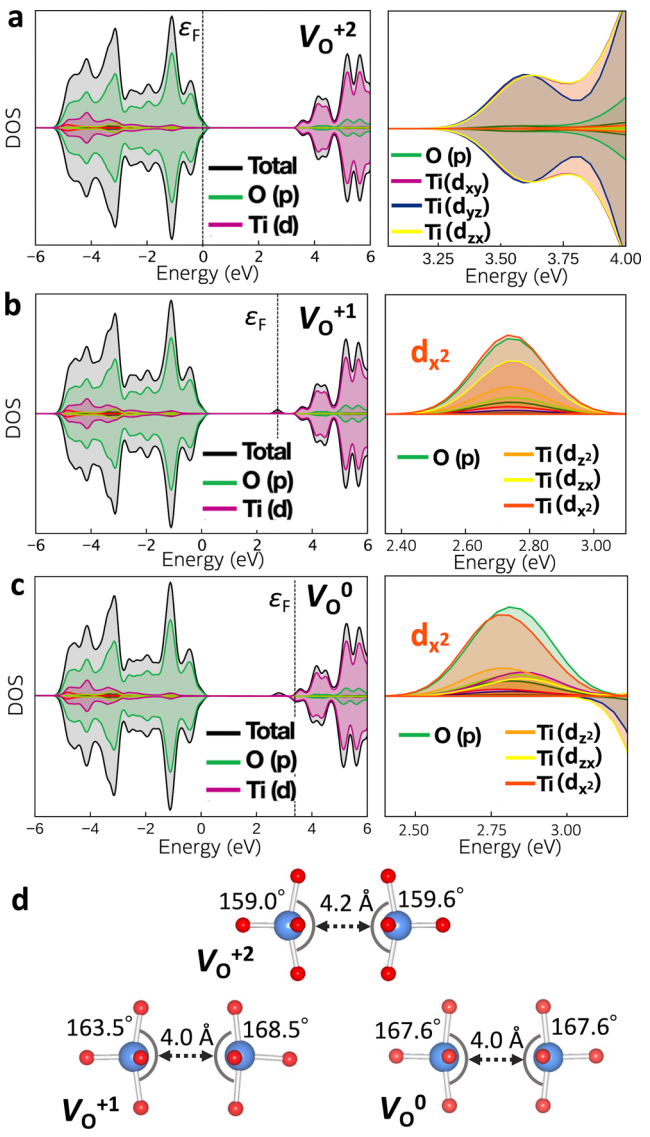

Figure 3. Electronic densities of states for $SrTiO_3$ supercells containing (a) V_O^{+2}, (b) V_O^{+1}, and (c) V_O^{0} with coordination environment of Ti atoms adjacent to the oxygen vacancy (d). The upper and lower panels in each DOS represent the majority and minority spins, respectively. The original Ti−Ti distance in the absence of oxygen vacancy is 3.9 Å.

Figure 3a shows the DOS of the supercell with the fully ionized V_O^{+2}, which represents the removal of O^{2-} and thus there are no excess electrons in the system. The lower conduction band is derived from Ti-3d t_{2g} orbitals (d_{xy}, d_{yz}, d_{zx}). The ground state V_O^{+2} structure involves two Ti atoms moving away from the oxygen vacancy, resulting in a Ti−Ti distance of 4.2 Å (Figure 3d). A similar geometry is found in other computational studies.[62,66,67] The removal of an oxide ion triggers a corresponding atomic displacement with two neighboring Ti ions repelled, due to the cleaved electrostatic attraction and orbital interaction. The deformation stabilizes the low coordination Ti sites via Ti 3d−O 2p interaction to form bonding−antibonding combinations directed away from the vacancy (as in the second-order Jahn−Teller effect) as shown in Figure 4a.[66,68]

In contrast to the fully ionized defect, V_O^{+1} and V_O^{0} exhibit occupied in-gap states associated with Ti^{3+} (Figure 3b,c). This is consistent with the experimental observations that the oxygen vacancy reduces Ti^{4+} to Ti^{3+} in $SrTiO_3$.[17] This in-gap state is contributed by Ti $3d_{x^2-y^2}$ from e_g, which cannot be explained by considering the coordination environment of only one Ti atom. As shown in Figure 4b, at the distorted Ti environment with an oxygen vacancy (with C_{4v} point symmetry), Ti $3d_{yz}$ from the t_{2g} set is the lowest energy molecular orbital. There are two Ti atoms adjacent to one oxygen vacancy, however. Here, the e_g orbitals ($d_{x^2-y^2}$) of the two Ti atoms are directed toward each other along the x-axis, to form the σ bonding−antibonding interaction (Figure 4c) as suggested previously.[69−71] For V_O^{+1} and V_O^{0}, the additional electrons occupy the bonding state, stabilizing the Ti−Ti interaction. When the interaction is strong enough, the σ bonding state ($d_{x^2-y^2}$) is lower than the $3d_{yz}$ (i.e., the original CBM), yielding the in-gap state. On the other hand, the Ti−Ti interaction is less favorable for V_O^{+2} because of the absence of electrons that can occupy the σ state as evidenced by greater Ti−Ti separation, making V_O^{+2} free from the in-gap state. While the cleavage of the O−Ti bonds at the vacancy site and resulting outward Ti displacements narrows the O−Ti−O angle, the Ti−Ti interaction favors reduced Ti−Ti distances and acts to widen the O−Ti−O angle (Figure 3d), giving competing effects. Although some computational studies report an O−Ti−O angle exceeding 180°,[63] such a structure is not stabilized with the present computational setup. Another possible state is one electron mostly localized on one Ti atom.[63] However, this polaronic state is slightly higher in energy than the Ti−Ti bonding state in the present calculation (Figure S6). From these results, we conclude that the origin of the in-gap state is the Ti 3d−Ti 3d bonding interaction across the oxygen vacancy. An analogue can be seen in the lead halide perovskites, where Pb 6p−Pb 6p σ bonding across the halide vacancy causes an in-gap state.[72]

This in-gap state formed with the oxygen vacancy is believed to deteriorate the activity of $SrTiO_3$ photocatalysts by trapping photoexcited electrons.[6,15,17,23] We evaluated the nonradiative carrier capture process when $SrTiO_3$ is subject to above band gap illumination within the framework of multiphonon emission,[73] i.e.,

$$V_O^{+2} \overset{h\nu}{\rightleftharpoons} V_O^{+2} + e^- + h^+ \overset{-\hbar\omega}{\rightleftharpoons} V_O^{+} + h^+ \overset{-\hbar\omega}{\rightleftharpoons} V_O^{+2} \quad (2)$$

where the excess electronic energy provided by light absorption ($h\nu$) is thermally emitted through phonons ($\hbar\omega$). The potential energy surface (PES) between V_O^{+2} and V_O^{+} was

https://doi.org/10.1021/jacs.5c07104
J. Am. Chem. Soc. XXXX, XXX, XXX−XXX

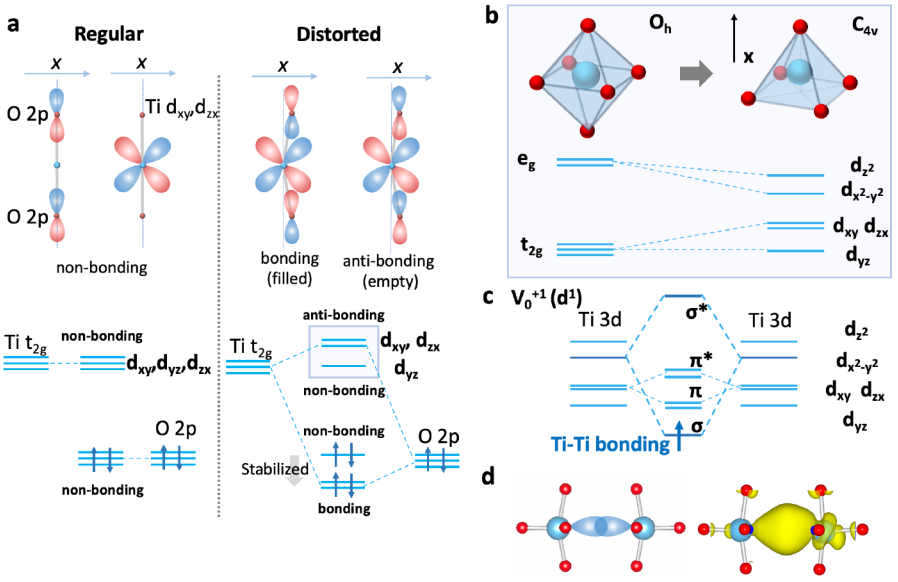

Figure 4. (a) Illustration of the band-edge orbital interaction in $SrTiO_3$. In a regular octahedral environment, the band edge O 2p and Ti 3d states are nonbonding. The oxygen vacancy allows for a distorted environment, which is stabilized by Ti−O bonding−antibonding interaction. (b) Resolved degeneracy of d-orbitals through the coordination environment change from O_h to C_{4v} accompanied by the oxygen vacancy. (c) Orbital interaction between two Ti atoms across the oxygen vacancy. The d_{z^2} orbitals directed toward each other interact to form σ and σ^* states, with the former corresponding to the in-gap trap state. (d) Schematic illustration of Ti 3d−Ti 3d interaction across the oxygen vacancy and calculated electron density map of the V_O^{+1}-induced in-gap state shown in Figure 3b (2.3−3.2 eV) is also shown (at an isosurface value of 2×10^{-3} e/Å^3). The uneven charge density distribution between the two Ti cations may arise from the competition between the orbital interaction (c), which favors charge distribution, and the Coulombic interaction, which favors electron localization.

calculated along the one-dimensional configuration coordinate Q defined as

$$Q^2 = \sum_{\alpha} M_{\alpha} \Delta R_{\alpha}^2 \tag{3}$$

where M_α and ΔR_α are the mass and the displacement of an atom α between the two configurations (Figure 5a). Based on these PES, the nuclear wave function overlaps were obtained via the 1D Schrödinger equation.[74,75] Combined with the electron−phonon coupling coefficient calculated within the static coupling approach,[73,76] we obtained the carrier capture cross sections $\sigma_{e/h}$. They show weak temperature dependence in the range up to 500 K (Figure S7). The small activation energy barrier (ΔE_e) and the Coulombic attraction between the positively charged V_O^{+2} and free electrons result in a large electron capture coefficient (C_e) of 5.6×10^{-8} cm^3 s^{-1} and cross-section (σ_e) of 3.6×10^{-15} cm^2 at room temperature (Table S6), suggesting fast electron capture by the oxygen vacancy. On the other hand, the hole capture is much slower with a capture coefficient (C_h) of 9.5×10^{-23} cm^3 s^{-1} and cross-section (σ_h) of 7.4×10^{-30} cm^2. These results are consistent with an experimental observation of a long hole lifetime even after the fast electron trapping producing Ti^{3+}, as revealed by transient absorption measurements.[77] The trapping not only immobilizes (i.e., localizes) the electrons but also lowers their energetic potential. Given the relatively small overpotential for the water reduction, i.e., the CBM position vs RHE of $SrTiO_3$ (0.4−0.8 eV),[78,79] the energy loss by trapping (~0.4 eV) can be extremely detrimental for water splitting photocatalytic activity by limiting the H_2O reduction process.

Effect of Al Doping. There are several mechanisms through which Al can reduce the trap density in $SrTiO_3$. One indirect route is to lower the Fermi level through Al^{3+} replacement of Ti^{4+}, which can affect the self-consistent concentration of V_O. Another mechanism involves the direct modification of the electronic structure and defect chemistry at the V_O site.

Al can be substitutional on Sr or Ti sites (Al_{Sr}, Al_{Ti}), or may form an interstitial (Al_i). The formation energies of Al_{Sr}, Al_{Ti}, and Al_i are calculated for the oxygen-poor limit (Figure 6a). Considering the flux synthesis of $SrTiO_3$:Al at ~1400 K in the molten salt of $SrCl_2$ (Figures S8 and S9), the Sr-rich condition with $\Delta\mu_O = -3$ eV is also investigated (denoted as condition **h**; Figure 1b). $\Delta\mu_{Al}$ is determined by $SrAl_2O_4$ as a competing phase, assuming an Al-rich condition for both cases. When ε_F is near the CBM, the main Al-related species is Al_{Ti}^{-1}, consistent with the experimentally intended species.

The effect of the Al dopant concentration on ε_F and the V_O species is calculated by changing the $\Delta\mu_{Al}$ and, thereby, the corresponding Al concentration at each condition. As shown in Figure 6, under both conditions, Al doping slightly lowers ε_F because of the electron compensation by the substitutional Al defect (Al_{Ti}^{-1}). The Fermi level lowering increases the V_O^{+1} and V_O^{+2} concentrations (Figure 6c,f). The experimental dopant concentration is reported to be around 1% atomic ratio to the Ti site.[15,23] As expected from the negative charge of the main defect species (Al_{Ti}^{-1}), Al doping increases the total concentration of positively charged V_O states, which cannot explain the observed in-gap state passivation by Al doping. In addition, Al_{Ti} itself can act as a hole trap (Figure 5b), consistent with photocatalytic activity lowering with excessive Al doping.[14] Thus, isolated Al_{Ti} cannot explain the increased photocatalytic activity of $SrTiO_3$ induced by Al doping.

Formation of a Defect Complex. Another possibility is that the electronic structure is changed by Al association with V_O.[17,80] A complex would be stabilized by the Coulombic attraction between positively charged $V_O^{+1/+2}$ and Al_{Ti}^{-1}, as

https://doi.org/10.1021/jacs.5c07104
J. Am. Chem. Soc. XXXX, XXX, XXX−XXX

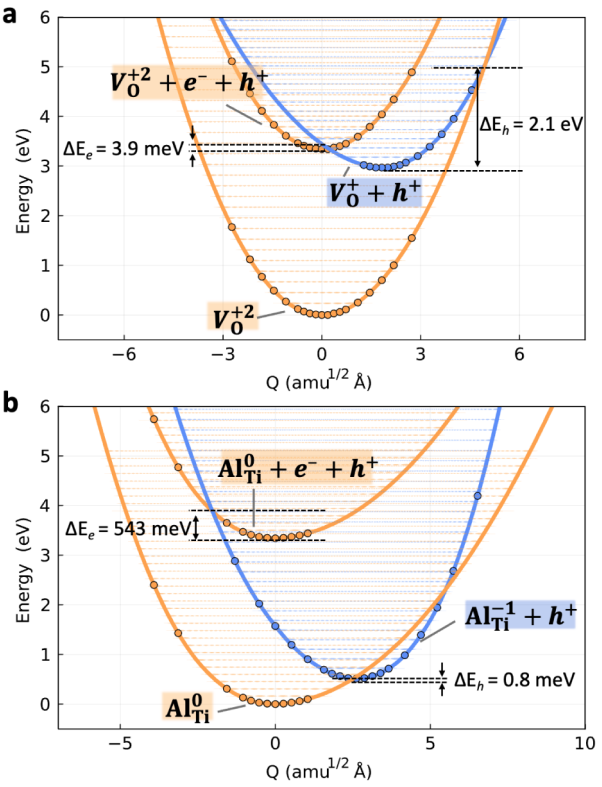

Figure 5. Potential energy surface (PES) for charge transition between (a) V_O^{+2} and (b) V_O^+ and Al_{Ti}^0 and Al_{Ti}^{-1} in $SrTiO_3$. The transition from the upper orange PES (V_O^{+2} (Al_{Ti}^0) + e^- + h^+) to the middle blue PES (V_O^+ (Al_{Ti}^{-1}) + h^+) corresponds to electron capture by V_O^{+2} (Al_{Ti}^0), while that from the middle blue to the lower orange PES (V_O^{+2} (Al_{Ti}^0)) corresponds to hole capture by V_O^+ (Al_{Ti}^{-1}). $\Delta E_{h/e}$ denotes the activation energy barrier to hole/electron capture.

well as the high concentrations of oxygen vacancies and Al dopants (thus lower entropic cost to complex formation).[52,81]

Here, Al_{Ti} exhibits the lowest formation energy for Al-related point defects when ε_F is near the CBM (Figure 6). When forming a complex with oxygen vacancies [V_O-Al_{Ti}], Al prefers to replace Ti adjacent to the oxygen vacancy (Figure S10). The complex binding energy from two isolated defects, A + B ⇌ AB, is given by

$$\Delta E = E^f(\mathrm{AB}) - (E^f(\mathrm{A}) + E^f(\mathrm{B})) \quad (4)$$

where E^f(A), E^f(B) and E^f(AB) are the formation energies of isolated defects A, B and a complex AB as determined from eq 1. We consider the following three association reaction retaining the total charge for simplicity:

$$V_O^0 + Al_{Ti}^{-1} \rightleftharpoons [V_O - Al_{Ti}]^{-1} \qquad \Delta E = -0.29\ \mathrm{eV} \quad (5)$$

$$V_O^{+1} + Al_{Ti}^{-1} \rightleftharpoons [V_O - Al_{Ti}]^{0} \qquad \Delta E = -0.64\ \mathrm{eV} \quad (6)$$

$$V_O^{+2} + Al_{Ti}^{-1} \rightleftharpoons [V_O - Al_{Ti}]^{+1} \qquad \Delta E = -0.90\ \mathrm{eV} \quad (7)$$

The more negative ΔE for the higher charge of V_O is due to the stronger Coulomb interaction. Complex formation is exothermic in all three cases.

The equilibrium constant for complexation can be approximated from the mass-action law:[81]

$$K = \frac{C_{AB}}{C_A C_B} = \frac{N_{AB}}{N_A N_B} \exp\left(-\frac{\Delta E}{k_B T}\right) \quad (8)$$

where C_A, C_B and C_{AB} are concentrations of defects and N_A, N_B and N_{AB} are the number of available states. Herein, N_{states} for [V_O-Al_{Ti}] except for the spin contribution is approximated to be twice that of V_O considering the two adjacent Ti where Al can be introduced. Let us now consider the case where the isolated defects are formed during the annealing process at a high temperature (1400 K in the present case), and they

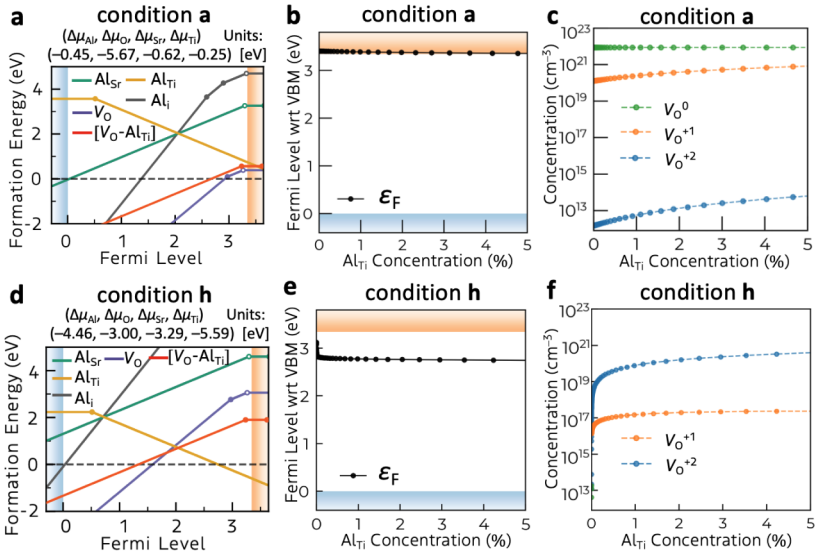

Figure 6. (a, d) Formation energies and transition level diagrams of Al dopant species, oxygen vacancy, and the defect complex (oxygen vacancy + Al substitution on Ti) in $SrTiO_3$ under condition **a** (oxygen poor limit) and condition **h** ($\Delta\mu_O$ = −3 eV). In both cases, Al-rich conditions are assumed, where the upper limits of $\Delta\mu_{Al}$ are set to −0.45 eV and −4.46 eV for conditions **a** and **h**, respectively, given $SrAl_2O_4$ as the bordering phase. (b, e) The effect of Al dopant concentration on the self-consistent Fermi levels. (c, f) The corresponding concentration of each charge state of V_O when the system is annealed at 1400 K and cooled to room temperature. For reference, the experimental Al dopant concentration in $SrTiO_3$:Al is ∼1 at%.

https://doi.org/10.1021/jacs.5c07104
J. Am. Chem. Soc. XXXX, XXX, XXX−XXX

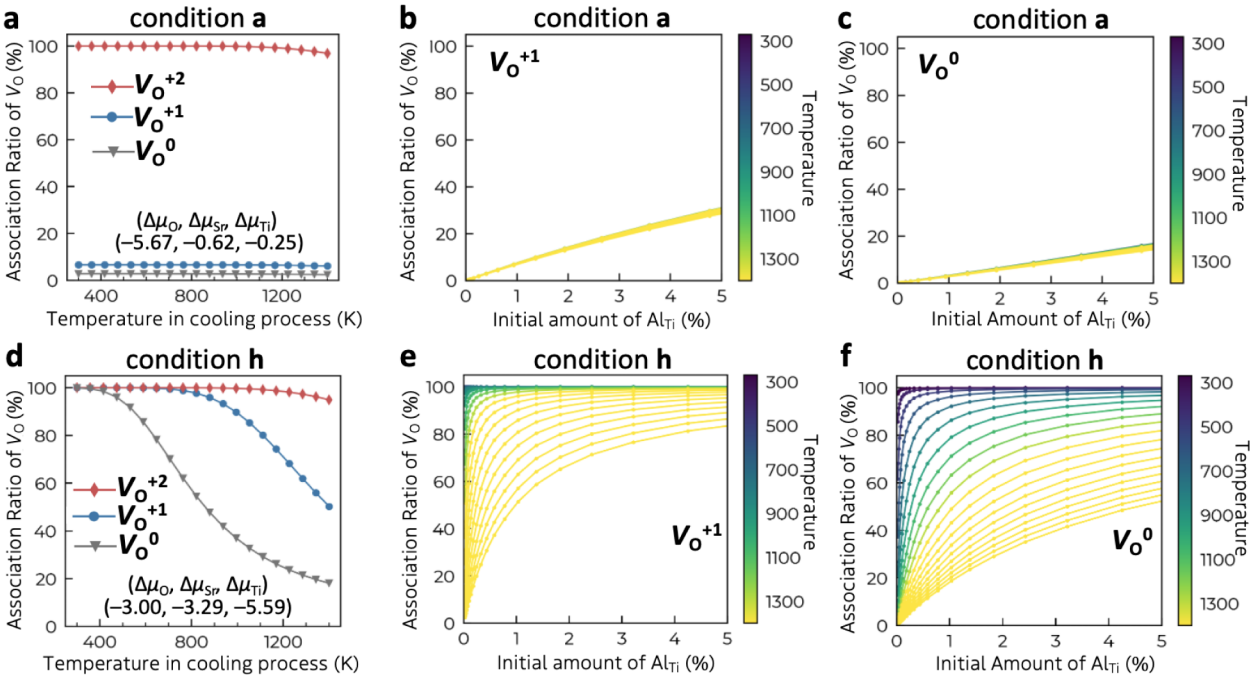

Figure 7. (a, d) Ratio of the concentration of the $[V_O\text{-}Al_{Ti}]^0$ complex to the initial concentration of V_O (i.e., the association ratio) under condition **a** (oxygen poor limit) and condition **h** ($\Delta\mu_O = -3$ eV). We considered the case where the isolated defects are formed during the annealing process at 1400 K, and they associate with each other at a certain lower temperature. The initial concentration of Al_{Ti} at 1400 K is fixed to 1 at%. Dependency of V_O association ratio on the initial concentration of Al_{Ti} at (b, c) condition **a** and (e, f) condition **h**.

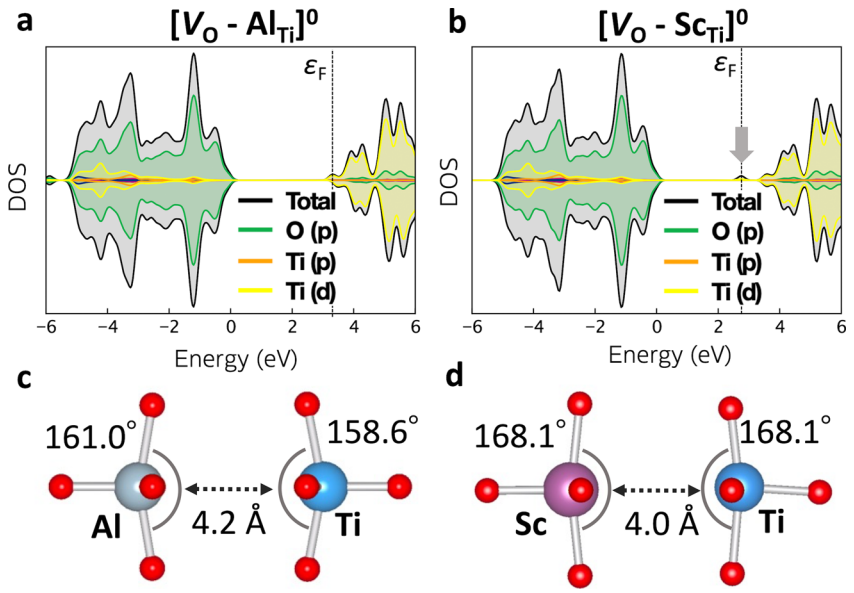

Figure 8. Electronic density of states for $SrTiO_3$ containing defect complex (a) $[V_O\text{-}Al_{Ti}]^0$, (b) $[V_O\text{-}Sc_{Ti}]^0$ with (c, d) the respective atomic geometries around the oxygen vacancy.

associate with each other at a certain lower temperature. The initial concentration of V_O (C_A^{ini}) at 1400 K is determined by the self-consistent defect calculation under a given chemical potential condition, where $\Delta\mu_{Al}$ was determined to make the C_B^{ini} equal to 1% of the Ti site density in $SrTiO_3$. Equation 8 is solved under the conditions that $C_A^{ini} = C_A + C_{AB}$ and $C_B^{ini} = C_B + C_{AB}$ are fixed.

The calculated association ratio of the oxygen vacancy is shown in Figures 7a,d and S11. While Vo^{+2} is mostly associated with Al_{Ti} at low temperatures under the oxygen-poor limit (condition **a**), V_O^{+1} and V_O^0 remain unassociated due to the excess amount of V_O relative to Al_{Ti}^{-1} (1 at%). The initial concentration of V_O^0 (5.3×10^{21} cm^{-3}) is much higher than that of Al_{Ti}^{-1} (1.7×10^{20} cm^{-3}). To increase the association ratio at the oxygen-poor limit, the initial amount of Al_{Ti}^{-1} could be increased. However, ~80% of V_O^0 is still unassociated even when 5 at% of Al_{Ti}^{-1} is introduced (Figure 7c). On the other hand, when the concentration of V_O^0 is lower under more oxygen-rich conditions (condition **h**), all the V_O species are associated with Al_{Ti}^{-1} (1 at%) as shown in Figure 7d–f.

https://doi.org/10.1021/jacs.5c07104
J. Am. Chem. Soc. XXXX, XXX, XXX−XXX

The effectiveness of Al doping therefore depends on the atmosphere and the synthetic temperature.

Although the precise chemical potential during actual synthesis is difficult to determine, the influence of oxygen partial pressure within the ideal gas approximation (Figure S8) shows that even a high vacuum condition ($\sim 10^{-12}$ atm) provides $\Delta\mu_O$ of ~ -3.5 eV at 1400 K. In addition, the experimentally observed downward ε_F shift with Al doping (0.5 eV) agrees with the downward shift at condition **h** (i.e., Sr-rich condition with $\Delta\mu_O = -3$ eV) of ~0.4 eV, as shown in Figure 6e. Therefore, the actual synthesis condition might be more oxygen-rich than the oxygen-poor limit ($\Delta\mu_O$ of −5.7 eV), and nearly all the V_O can be associated with Al_{Ti} even when the Al doping amount is 1 at% (Figure 7d for condition **h**).

The electronic states of V_O change upon association with Al_{Ti}. The in-gap states observed in V_O^{+1} and V_O^{0} are removed regardless of the charge state (Figures 8 and S12), making the trap level shallower (Figure 6a,d). As mentioned above, the in-gap state originates from the Ti 3d−Ti 3d interaction across the oxygen vacancy (Figure 4). Here, Al ($3s^2p^1$) does not possess d-orbitals as valence orbitals. Therefore, replacing one Ti adjacent to the oxygen vacancy with Al deactivates the Ti 3d−Ti 3d interaction, eliminating the in-gap state. The Al−Ti distance is larger than Ti−Ti distance in V_O^{+1} and V_O^{0}, reflecting the absence of the bonding interaction between them. While the isolated V_O acts as a carrier capture center that can deteriorate the photocatalytic activity (Figure 5), the defect complex removes the in-gap states. This removal of trapping and recombination channels explains the significant photocatalytic activity enhancement in Al-doped $SrTiO_3$ observed experimentally.[14,23]

Previous studies have stressed that the key to improving the photocatalytic activity is the lower valency of Al^{3+} compared to Ti^{4+}. This conclusion is supported from the improved activity by Al^{3+}, Ga^{3+}, and Mg^{2+} and the lowered activity by Ta^{5+}.[6] However, these cations can be classified also by the absence (Ga ($4s^2p^1$, Mg ($3s^2$)) or presence (Ta ($5d^36s^2$)) of the d valence orbitals. We propose that the frontier orbital compatibility is also a key factor. To illustrate this point, Sc ($3d^14s^2$) doping was also investigated. Sc^{3+} has a lower valency than Ti^{4+} but with d valence orbitals. The negative complex binding energy ($\Delta E = -0.36$ eV) shows that Sc_{Ti}^{+1} associates favorably with V_O^{-1}, as indicated previously.[82] As shown in Figure 8b, Sc_{Ti} does not eliminate the localized in-gap state when complexed with V_O. The Sc 3d can interact with Ti 3d orbitals as suggested by the shorter Sc−Ti distance compared to Al−Ti (Figure 8c, d) and the emergence of an associated in-gap electronic state. We note that the lower valence of the dopant is also required to provide an electrostatic driving force for complexation.

CONCLUSION

The oxygen vacancy in $SrTiO_3$ results in a detrimental defect state that traps photoexcited electrons. The origin of the trap state is a Ti 3d-Ti 3d interaction across the oxygen vacancy, whose bonding combination is stabilized within the band gap. We conclude that Al is preferentially incorporated substitutionally on Ti sites. Isolated Al_{Ti} acts as a hole capture site. However, the beneficial effect of Al emerges via the formation of [V_O-Al_{Ti}] complexes that eliminate the trap states. Replacing one Ti with Al without d valence orbitals deactivates the d-d interaction across the oxygen vacancy from which the in-gap state is derived. While the lower valency of Al helps to form the complex, it is insufficient to passivate the in-gap state. This is illustrated by Sc doping, where the Sc 3d−Ti 3d interaction does not eliminate the vacancy-induced in-gap states. The absence of d valence orbitals in the dopant is found to be key. The present study not only reveals the functional mechanism of Al doping to $SrTiO_3$, but also provides a strategy from the viewpoint of orbital interactions to "externally" impart the defect-tolerance to even conventional semiconductors by passivating in-gap trap states that hinder solar-to-electrical energy conversion.

EXPERIMENTAL SECTION

First-Principles Calculations. All first-principles calculations were performed using the projector augmented-wave (PAW) method[83] under three-dimensional periodic boundary conditions as implemented in the Vienna Ab Initio Simulation Package (VASP).[84−86] PAW data sets with radial cutoffs of 1.3, 1.2, 0.8, and 1.0 Å for Sr, Ti, O, and Al, respectively, were employed, where Sr (4s, 4p, 5s), Ti (3p, 4s, 3d), O (2s, 2p), and Al (3s, 3p) were treated as valence electrons. The HSE06 hybrid exchange-correlation functional[36] was used, which provides a good agreement in the band gap with experiment (Table S1). The plane-wave cutoff energy and Γ-centered *k*-point mesh were sequentially increased using the vaspup2.0 package[87] until the total energies from static calculations were converged to within 1 meV/atom. The given values were 600 eV and 5 × 5 × 5 for the 5-atom primitive cell of $SrTiO_3$. The atomic positions were optimized until the Hellman−Feynman forces on each atom were below 0.01 eV $Å^{-1}$. The energy convergence criterion was set to 10^{-6} eV. The ionic dielectric response was calculated by density functional perturbation theory[88] using the Perdew−Burke−Ernzerhof (PBE) formulation of the generalized gradient approximation (GGA) functional,[89] while the electronic contribution was calculated using the approach developed by Furthmüller et al.[88] with HSE06 functional. Electronic band structure diagrams were generated and analyzed using the sumo package.[90] Crystal orbital Hamilton populations (COHPs) were calculated using the LOBSTER package.[91]

Defect Modeling. In the present study, we employed the supercell formalism for computing defect energetics. The formation energy of a defect X in charge state q, $E^f_{X,q}(\varepsilon_F, \mu)$, is given as[41−43]

$$E^f_{X,q}(\varepsilon_F, \mu) = E_{X,q} - [E_H + \sum_i n_i\mu_i + q\cdot(-\varepsilon_F)] + E_{corr}(q) \quad (9)$$

where the total number of elements and electrons are conserved between $E_{X,q}$ and $[E_H + \sum_i n_i\mu_i + q\cdot(-\varepsilon_F)]$. A 135-atom supercell from a 3 × 3 × 3 expansion of the cubic $SrTiO_3$ conventional cell was used to minimize the interactions between the periodically repeated defects under three-dimensional periodic boundary conditions. Note that an odd supercell expansion is used for $SrTiO_3$ to "lock" the cubic structure[63] by restricting octahedral tilting[92] (see Figures S13 and S14). Local relaxation of the rattled bulk supercell with fixed volume does not find a lower energy structure. While a better approximation of the cubic structure, and response to defect formation, could be obtained from structural ensembles through molecular dynamics simulations, the computational cost would be prohibitively expensive at the present time. The ShakeNBreak approach[48,49] was used to initially generate Γ-point-only relaxations for each defect with 10 different local distortions, where more stable defect structures than the unperturbed ones were often found (Figures S15−S17). The ground state structure found in the initial relaxation was further optimized with a 2 × 2 × 2 *k*-point mesh to obtain the total energy of a defect structure. The extended Freysoldt−Neugebauer−Van de Walle (eFNV) correction scheme was also employed,[44,45] using a calculated static dielectric constant of 6.33.

The formation energy of each defect species $E^f_{X,q}(\varepsilon_F, \mu)$ depends on the Fermi level according to eq 9); $E^f_{X,q}(\varepsilon_F, \mu) \propto q\varepsilon_F$. At a certain

https://doi.org/10.1021/jacs.5c07104
J. Am. Chem. Soc. XXXX, XXX, XXX−XXX

Fermi level $\varepsilon_F$and temperature T, the concentration of defect X in charge state q ($C_{X,q}$) including the effect of the defects competing for the same site is given by[93,94]

$$C_{X,q} = N_{\text{site}}^{X} \frac{N_{\text{config}}^{X,q} \exp\left(-\frac{E_{X,q}^{f}(\varepsilon_F,\mu)}{k_B T}\right)}{1 + \sum_{X'} \sum_{q'} N_{\text{config}}^{X',q'} \exp\left(-\frac{E_{X',q'}^{f}(\varepsilon_F,\mu)}{k_B T}\right)} \tag{10}$$

where N_{site}^{X} is the density of lattice sites on which the defect X can form, while N_{config} is the number of equivalent configurations (degeneracy) at each site.[95,96] N_{config} is estimated by the point symmetry change around the defect site and the spin degeneracy (Table S4).[39] The sum in the denominator is performed over all defects (with charge q') that compete for the same site as defect X. Note that when the concentration of defects is small enough (i.e., $E_{X',q'}^{f} \gg k_B T$), eq 10 reaches a Boltzmann distribution:

$$C_{X,q} = N_{\text{site}}^{X} N_{\text{config}}^{X,q} \exp\left(-\frac{E_{X,q}^{f}(\varepsilon_F,\mu)}{k_B T}\right) \tag{11}$$

Although the Fermi level ε_F is a free variable in eq 9), it is fixed by the charge neutrality condition:

$$p - n + \sum_{X} \sum_{q} q C_{X,q} = 0 \tag{12}$$

where p and n are the concentrations of free holes and electrons in the valence and conduction bands. Not only $C_{X,q}C_{X,q}$ but n and p also depend on the Fermi level:

$$n = \int_{\varepsilon_C}^{\infty} f_e(\varepsilon)\rho(\varepsilon)\mathrm{d}\varepsilon; \quad f_e(\varepsilon) = \frac{1}{1 + \exp\left(\frac{\varepsilon - \varepsilon_F}{k_B T}\right)} \tag{13}$$

$$p = \int_{-\infty}^{\varepsilon_V} f_h(\varepsilon)\rho(\varepsilon)\mathrm{d}\varepsilon; \quad f_h(\varepsilon) = 1 - \frac{1}{1 + \exp\left(\frac{\varepsilon - \varepsilon_F}{k_B T}\right)} \tag{14}$$

where ε_V, ε_C are the VBM and CBM energies, $\rho(\varepsilon)$ is the electronic density-of-states, and $f_e(\varepsilon)$ is the Fermi−Dirac distribution function. As $C_{X,q}$, p and n depend on ε_F, ε_F is self-consistently determined by eq 12.[50,51]

The carrier and defect concentrations as a function of anneal temperature and chemical potential were estimated using the frozen defect approximation to mimic a synthetic condition where the material is annealed under elevated temperatures and cooled rapidly to room temperature.[51,52] Defects are formed at the elevated annealing temperature but remain during cooling due to the assumed large kinetic barriers for diffusion and annihilation. Using the total concentration of each defect fixed to that at the annealing temperature, ε_F is self-consistently calculated at room temperature (T = 300 K) where relative populations of defect charge states and carrier concentrations are re-equilibrated. The temperature dependence of the band gap (at annealing temperatures) was approximated using the experimentally reported band gap renormalization,[53] and assuming symmetric shifts in the valence and conduction band edges while keeping the defect levels fixed. The doped Python package was used to manage all the defect calculations and analysis.[39]

The chemical potential of oxygen μ_O (T, P_r) is obtained based on the results of the HSE06 hybrid functional calculation of an O_2 molecule (triplet state) in a supercell (30 Å × 30 Å × 30 Å), where P_r is the reference pressure (1 atm). The translational, electronic, rotational and vibrational contributions at each temperature are calculated by vaspkit.[97] Then $\mu_O(T, P)$ was obtained as follows:

$$\mu_{O_2}(T, P) = \mu_{O_2}(T, P_r) + k_B T \ln \frac{P}{P_r} \tag{15}$$

$$\mu_O(T, P) = \frac{1}{2}\mu_{O_2}(T, P) \tag{16}$$

Nonradiative Carrier Capture. The nonradiative carrier capture was simulated within the framework of multiphonon emission (MPE) using an extension of the method of Alkauskas et al.[73] to account for anharmonicity. The carrier capture coefficient can be expressed using Fermi's golden rule within linear electron−phonon coupling and first-order perturbation approximation, and one-dimensional configuration coordinate approach[73]

$$\tilde{C} = \frac{2\pi}{\hbar} V g W_{if}^2 \sum_{m} \omega_m \sum_{n} \left|\left\langle \chi_{im} | Q - Q_0 | \chi_{fn} \right\rangle\right|^2 \delta(\Delta E + m\hbar\Omega_i - n\hbar\Omega_f) \tag{17}$$

where V is the volume of the supercell, g is the degeneracy factor of the final state. ω_m is the thermal occupation of the vibrational state m of the initial state. ΔE is the energy difference between the initial and final state and $\Omega_{\{i,f\}}$ are the phonon frequencies of initial and final states. Q is defined as the one-dimensional configuration coordinate between the initial and final structures:

$$Q^2 = \sum_{\alpha} M_\alpha \Delta R_\alpha^2 \tag{18}$$

where M_α and ΔR_α are the mass and the displacement of an atom α between the two configurations. The electron−phonon coupling matrix is expressed as

$$W_{if} = \left\langle \psi_i \left| \frac{\partial \hat{h}}{\partial Q} \right| \psi_f \right\rangle \tag{19}$$

where ψ_j and $\hat{h}$ are the single-particle wave function and generalized Kohn−Sham Hamiltonian with the HSE06 hybrid functional, which is computed using nonrad[76] within PAW formalism. CarrierCapture.jl[74,75,98] was used to fit the potential energy surfaces (PES) and solve the 1D vibrational Schrödinger equation. The Sommerfeld parameter $s(T)$[99] is considered to account for the Coulombic interaction between the electron/hole and charged defect. When a defect supercell used to calculate W_{if} is charged, another scaling factor f is considered to correct the charged supercell effect.[76] The scaled carrier capture coefficient is given as

$$C = s(T) f \tilde{C} \tag{20}$$

The capture cross-section is given by

$$\sigma = C/\langle v \rangle \tag{21}$$

where $\langle v \rangle = \sqrt{3k_B T/m^*}$ is the average thermal velocity of the carrier and m^* is the average effective mass of electron/hole.

■ ASSOCIATED CONTENT

Data Availability Statement

All relevant data generated in the course of this work is freely available at 10.5281/zenodo.15493773.

Supporting Information

The Supporting Information is available free of charge at https://pubs.acs.org/doi/10.1021/jacs.5c07104.

Additional theoretical calculation results, including the formation energy of every defect and transition level diagram at every chemical potential conditions (PDF)

https://doi.org/10.1021/jacs.5c07104
J. Am. Chem. Soc. XXXX, XXX, XXX−XXX

AUTHOR INFORMATION

Corresponding Author

Kanta Ogawa − *Department of Materials, Imperial College London, London SW7 2AZ, United Kingdom; Materials and Structures Laboratory, Institute of Integrated Research, Institute of Science Tokyo, Yokohama 226-8501, Japan; Laboratory for Materials and Structures, Institute of Innovative Research, Tokyo Institute of Technology, Yokohama 226-8501, Japan;* Present Address: Department of Chemistry, Graduate School of Science, Kyoto University, Kitashirakawa Oiwake, Sakyo, Kyoto, Japan, 606-8502; orcid.org/0000-0002-6995-9848; Email: ogawa.kanta.3y@kyoto-u.ac.jp

Authors

Seán R Kavanagh − *Harvard University Center for the Environment, Harvard University, Cambridge, Massachusetts 02138, United States;* orcid.org/0000-0003-4577-9647

Fumiyasu Oba − *Materials and Structures Laboratory, Institute of Integrated Research, Institute of Science Tokyo, Yokohama 226-8501, Japan; Laboratory for Materials and Structures, Institute of Innovative Research, Tokyo Institute of Technology, Yokohama 226-8501, Japan;* orcid.org/0000-0001-7178-5333

Aron Walsh − *Department of Materials, Imperial College London, London SW7 2AZ, United Kingdom;* orcid.org/0000-0001-5460-7033

Complete contact information is available at: https://pubs.acs.org/10.1021/jacs.5c07104

Notes

The authors declare no competing financial interest.

ACKNOWLEDGMENTS

This work was supported by the JSPS overseas program and JSPS KAKENHI Grant Numbers JP24KJ1044, JP24K21683 and JP24H00376. Via the authors' membership of the UK's HEC Materials Chemistry Consortium, which is funded by EPSRC (EP/X035859/1), this work used the ARCHER2 UK National Supercomputing Service (http://www.archer2.ac.uk). The supercomputer of ACCMS at Kyoto University and the TSUBAME4.0 supercomputer at Institute of Science Tokyo were also used for this work. SRK acknowledges the Harvard University Center for the Environment (HUCE) for funding a fellowship.

REFERENCES

(1) Domen, K.; Naito, S.; Soma, M.; Onishi, T.; Tamaru, K. Photocatalytic Decomposition of Water Vapour on an NiO−$SrTiO_3$ Catalyst. *J. Chem. Soc., Chem. Commun.* **1980**, No. 12, 543−544.

(2) Lehn, J.-M.; Sauvage, J.-P.; Ziessel, R. Photochemical water splitting. Continuous generation of hydrogen and oxygen by irradiation of aqueous suspensions of metal loaded strontium titanate. *Nouv. J. Chim.* **1980**, *4* (11), 624−627.

(3) Wagner, F. T.; Somorjai, G. A. Photocatalytic and Photoelectrochemical Hydrogen Production on Strontium Titanate Single Crystals. *J. Am. Chem. Soc.* **1980**, *102* (17), 5494−5502.

(4) Kato, H.; Kudo, A. Visible-Light-Response and Photocatalytic Activities of TiO_2 and $SrTiO_3$ Photocatalysts Codoped with Antimony and Chromium. *J. Phys. Chem. B* **2002**, *106* (19), 5029−5034.

(5) Konta, R.; Ishii, T.; Kato, H.; Kudo, A. Photocatalytic Activities of Noble Metal Ion Doped $SrTiO_3$ under Visible Light Irradiation. *J. Phys. Chem. B* **2004**, *108* (26), 8992−8995.

(6) Takata, T.; Domen, K. Defect Engineering of Photocatalysts by Doping of Aliovalent Metal Cations for Efficient Water Splitting. *J. Phys. Chem. C* **2009**, *113* (45), 19386−19388.

(7) Kato, H.; Kobayashi, M.; Hara, M.; Kakihana, M. Fabrication of $SrTiO_3$ Exposing Characteristic Facets Using Molten Salt Flux and Improvement of Photocatalytic Activity for Water Splitting. *Catal. Sci. Technol.* **2013**, *3* (7), 1733.

(8) Yamakata, A.; Yeilin, H.; Kawaguchi, M.; Hisatomi, T.; Kubota, J.; Sakata, Y.; Domen, K. Morphology-Sensitive Trapping States of Photogenerated Charge Carriers on $SrTiO_3$ Particles Studied by Time-Resolved Visible to Mid-IR Absorption Spectroscopy: The Effects of Molten Salt Flux Treatments. *J. Photochem. Photobiol., A* **2015**, *313*, 168−175.

(9) Mu, L.; Zhao, Y.; Li, A.; Wang, S.; Wang, Z.; Yang, J.; Wang, Y.; Liu, T.; Chen, R.; Zhu, J.; Fan, F.; Li, R.; Li, C. Enhancing Charge Separation on High Symmetry $SrTiO_3$ Exposed with Anisotropic Facets for Photocatalytic Water Splitting. *Energy Environ. Sci.* **2016**, *9* (7), 2463−2469.

(10) Townsend, T. K.; Browning, N. D.; Osterloh, F. E. Overall Photocatalytic Water Splitting with NiO_x−$SrTiO_3$ − a Revised Mechanism. *Energy Environ. Sci.* **2012**, *5* (11), 9543.

(11) Chiang, T. H.; Lyu, H.; Hisatomi, T.; Goto, Y.; Takata, T.; Katayama, M.; Minegishi, T.; Domen, K. Efficient Photocatalytic Water Splitting Using Al-Doped $SrTiO_3$ Coloaded with Molybdenum Oxide and Rhodium−Chromium Oxide. *ACS Catal.* **2018**, *8* (4), 2782−2788.

(12) Mu, L.; Zeng, B.; Tao, X.; Zhao, Y.; Li, C. Unusual Charge Distribution on the Facet of a $SrTiO_3$ Nanocube under Light Irradiation. *J. Phys. Chem. Lett.* **2019**, *10* (6), 1212−1216.

(13) Han, K.; Haiber, D. M.; Knöppel, J.; Lievens, C.; Cherevko, S.; Crozier, P.; Mul, G.; Mei, B. CrO_x -Mediated Performance Enhancement of Ni/NiO-Mg: $SrTiO_3$ in Photocatalytic Water Splitting. *ACS Catal.* **2021**, *11* (17), 11049−11058.

(14) Ham, Y.; Hisatomi, T.; Goto, Y.; Moriya, Y.; Sakata, Y.; Yamakata, A.; Kubota, J.; Domen, K. Flux-Mediated Doping of $SrTiO_3$ Photocatalysts for Efficient Overall Water Splitting. *J. Mater. Chem. A* **2016**, *4* (8), 3027−3033.

(15) Takata, T.; Jiang, J.; Sakata, Y.; Nakabayashi, M.; Shibata, N.; Nandal, V.; Seki, K.; Hisatomi, T.; Domen, K. Photocatalytic Water Splitting with a Quantum Efficiency of Almost Unity. *Nature* **2020**, *581* (7809), 411−414.

(16) Nishiyama, H.; Yamada, T.; Nakabayashi, M.; Maehara, Y.; Yamaguchi, M.; Kuromiya, Y.; Nagatsuma, Y.; Tokudome, H.; Akiyama, S.; Watanabe, T.; Narushima, R.; Okunaka, S.; Shibata, N.; Takata, T.; Hisatomi, T.; Domen, K. Photocatalytic Solar Hydrogen Production from Water on a 100-m^2 Scale. *Nature* **2021**, *598* (7880), 304−307.

(17) Zhao, Z.; Goncalves, R. V.; Barman, S. K.; Willard, E. J.; Byle, E.; Perry, R.; Wu, Z.; Huda, M. N.; Moulé, A. J.; Osterloh, F. E. Electronic Structure Basis for Enhanced Overall Water Splitting Photocatalysis with Aluminum Doped $SrTiO_3$ in Natural Sunlight. *Energy Environ. Sci.* **2019**, *12* (4), 1385−1395.

(18) Bednorz, J. G.; Müller, K. A. Possible High Tc Superconductivity in the Ba-La-Cu-O System. *Z. Physik, B* **1986**, *64*, 189−193.

(19) Bel Hadj Tahar, R.; Ban, T.; Ohya, Y.; Takahashi, Y. Tin Doped Indium Oxide Thin Films: Electrical Properties. *J. Appl. Phys.* **1998**, *83* (5), 2631−2645.

(20) Kamihara, Y.; Watanabe, T.; Hirano, M.; Hosono, H. Iron-Based Layered Superconductor $La[O_{1-x}F_x]FeAs$ (x = 0.05−0.12) with T_c = 26 K. *J. Am. Chem. Soc.* **2008**, *130* (11), 3296−3297.

(21) Kawasaki, S.; Akagi, K.; Nakatsuji, K.; Yamamoto, S.; Matsuda, I.; Harada, Y.; Yoshinobu, J.; Komori, F.; Takahashi, R.; Lippmaa, M.; Sakai, C.; Niwa, H.; Oshima, M.; Iwashina, K.; Kudo, A. Elucidation of Rh-Induced In-Gap States of Rh: $SrTiO_3$ Visible-Light-Driven Photocatalyst by Soft X-Ray Spectroscopy and First-Principles Calculations. *J. Phys. Chem. C* **2012**, *116* (46), 24445−24448.

(22) Ogawa, K.; Abe, R.; Walsh, A. Band Gap Narrowing by Suppressed Lone-Pair Activity of Bi^{3+}. *J. Am. Chem. Soc.* **2024**, *146* (9), 5806−5810.
(23) Goto, Y.; Hisatomi, T.; Wang, Q.; Higashi, T.; Ishikiriyama, K.; Maeda, T.; Sakata, Y.; Okunaka, S.; Tokudome, H.; Katayama, M.; Akiyama, S.; Nishiyama, H.; Inoue, Y.; Takewaki, T.; Setoyama, T.; Minegishi, T.; Takata, T.; Yamada, T.; Domen, K. A Particulate Photocatalyst Water-Splitting Panel for Large-Scale Solar Hydrogen Generation. *Joule* **2018**, *2* (3), 509−520.
(24) Zakutayev, A.; Caskey, C. M.; Fioretti, A. N.; Ginley, D. S.; Vidal, J.; Stevanovic, V.; Tea, E.; Lany, S. Defect Tolerant Semiconductors for Solar Energy Conversion. *J. Phys. Chem. Lett.* **2014**, *5* (7), 1117−1125.
(25) Zhang, X.; Turiansky, M. E.; Van De Walle, C. G. Correctly Assessing Defect Tolerance in Halide Perovskites. *J. Phys. Chem. C* **2020**, *124* (11), 6022−6027.
(26) Kavanagh, S. R.; Nielsen, R. S.; Hansen, J. L.; Davidsen, R. S.; Hansen, O.; Samli, A. E.; Vesborg, P. C. K.; Scanlon, D. O.; Walsh, A. Intrinsic Point Defect Tolerance in Selenium for Indoor and Tandem Photovoltaics. *Energy Environ. Sci.* **2025**, *18*, 4431−4446.
(27) Walsh, A.; Payne, D. J.; Egdell, R. G.; Watson, G. W. Stereochemistry of Post-Transition Metal Oxides: Revision of the Classical Lone Pair Model. *Chem. Soc. Rev.* **2011**, *40* (9), 4455.
(28) Brandt, R. E.; Stevanović, V.; Ginley, D. S.; Buonassisi, T. Identifying Defect-Tolerant Semiconductors with High Minority-Carrier Lifetimes: Beyond Hybrid Lead Halide Perovskites. *MRS Commun.* **2015**, *5* (2), 265−275.
(29) Ogawa, K.; Tolborg, K.; Walsh, A. Models of Oxygen Occupancy in Lead Phosphate Apatite $Pb_{10}(PO_4)_6O$. *ACS Energy Lett.* **2023**, *8* (9), 3941−3944.
(30) Zhang, S. B.; Wei, S.-H.; Zunger, A.; Katayama-Yoshida, H. Defect Physics of the $CuInSe_2$ Chalcopyrite Semiconductor. *Phys. Rev. B* **1998**, *57* (16), 9642.
(31) Kurchin, R. C.; Gorai, P.; Buonassisi, T.; Stevanović, V. Structural and Chemical Features Giving Rise to Defect Tolerance of Binary Semiconductors. *Chem. Mater.* **2018**, *30* (16), 5583−5592.
(32) Ogawa, K.; Suzuki, H.; Walsh, A.; Abe, R. Orbital Engineering in Sillén−Aurivillius Phase Bismuth Oxyiodide Photocatalysts through Interlayer Interactions. *Chem. Mater.* **2023**, *35* (14), 5532−5540.
(33) Ogawa, K.; Suzuki, H.; Zhong, C.; Sakamoto, R.; Tomita, O.; Saeki, A.; Kageyama, H.; Abe, R. Layered Perovskite Oxyiodide with Narrow Band Gap and Long Lifetime Carriers for Water Splitting Photocatalysis. *J. Am. Chem. Soc.* **2021**, *143* (22), 8446−8453.
(34) Mosquera-Lois, I.; Huang, Y.-T.; Lohan, H.; Ye, J.; Walsh, A.; Hoye, R. L. Z. Multifaceted Nature of Defect Tolerance in Halide Perovskites and Emerging Semiconductors. *Nat. Rev. Chem.* **2025**, *9*, 287.
(35) Ganose, A. M.; Scanlon, D. O.; Walsh, A.; Hoye, R. L. Z. The Defect Challenge of Wide-Bandgap Semiconductors for Photovoltaics and Beyond. *Nat. Commun.* **2022**, *13* (1), 4715.
(36) Krukau, A. V.; Vydrov, O. A.; Izmaylov, A. F.; Scuseria, G. E. Influence of the Exchange Screening Parameter on the Performance of Screened Hybrid Functionals. *J. Chem. Phys.* **2006**, *125* (22), 224106.
(37) van Benthem, K.; Elsässer, C.; French, R. H. Bulk Electronic Structure of $SrTiO_3$: Experiment and Theory. *J. Appl. Phys.* **2001**, *90* (12), 6156−6164.
(38) Cox, P. A. *The Electronic Structure and Chemistry of Solids*; Oxford Science Publications: Oxford, 1986.
(39) Kavanagh, S. R.; Squires, A. G.; Nicolson, A.; Mosquera-Lois, I.; Ganose, A. M.; Zhu, B.; Brlec, K.; Walsh, A.; Scanlon, D. O. Doped: Python Toolkit for Robust and Repeatable Chargeddefect Supercell Calculations. *JOSS* **2024**, *9* (96), 6433.
(40) Jain, A.; Ong, S. P.; Hautier, G.; Chen, W.; Richards, W. D.; Dacek, S.; Cholia, S.; Gunter, D.; Skinner, D.; Ceder, G.; Persson, K. A. Commentary: The Materials Project: A Materials Genome Approach to Accelerating Materials Innovation. *APL Mater.* **2013**, *1* (1), 011002.
(41) Freysoldt, C.; Grabowski, B.; Hickel, T.; Neugebauer, J.; Kresse, G.; Janotti, A.; Van De Walle, C. G. First-Principles Calculations for Point Defects in Solids. *Rev. Mod. Phys.* **2014**, *86* (1), 253−305.
(42) Goyal, A.; Gorai, P.; Peng, H.; Lany, S.; Stevanović, V. A Computational Framework for Automation of Point Defect Calculations. *Comput. Mater. Sci* **2017**, *130*, 1−9.
(43) Kim, S.; Hood, S. N.; Park, J.-S.; Whalley, L. D.; Walsh, A. Quick-Start Guide for First-Principles Modelling of Point Defects in Crystalline Materials. *arXiv*.
(44) Kumagai, Y.; Oba, F. Electrostatics-Based Finite-Size Corrections for First-Principles Point Defect Calculations. *Phys. Rev. B* **2014**, *89* (19), 195205.
(45) Freysoldt, C.; Neugebauer, J.; Van De Walle, C. G. Fully *Ab Initio* Finite-Size Corrections for Charged-Defect Supercell Calculations. *Phys. Rev. Lett.* **2009**, *102* (1), 016402.
(46) Kavanagh, S. R.; Walsh, A.; Scanlon, D. O. Rapid Recombination by Cadmium Vacancies in CdTe. *ACS Energy Lett.* **2021**, *6*, 1392−1398.
(47) Mosquera-Lois, I.; Kavanagh, S. R. In Search of Hidden Defects. *Matter.* **2021**, *4* (8), 2602−2605.
(48) Mosquera-Lois, I.; Kavanagh, S. R.; Walsh, A.; Scanlon, D. O. ShakeNBreak: Navigating the Defect Configurational Landscape. *JOSS* **2022**, *7* (80), 4817.
(49) Mosquera-Lois, I.; Kavanagh, S. R.; Walsh, A.; Scanlon, D. O. Identifying the Ground State Structures of Point Defects in Solids. *Npj Comput. Mater.* **2023**, *9* (1), 25.
(50) Buckeridge, J. Equilibrium Point Defect and Charge Carrier Concentrations in a Material Determined through Calculation of the Self-Consistent Fermi Energy. *Comput. Phys. Commun.* **2019**, *244*, 329−342.
(51) Squires, A. G.; Scanlon, D. O.; Morgan, B. J. Py-Sc-Fermi: Self-Consistent Fermi Energies and Defect Concentrations from Electronic Structure Calculations. *JOSS* **2023**, *8* (82), 4962.
(52) Cen, J.; Zhu, B.; Kavanagh, S. R.; Squires, A. G.; Scanlon, D. O. Cation Disorder Dominates the Defect Chemistry of High-Voltage $LiMn_{1.5}Ni_{0.5}O_4$ (LMNO) Spinel Cathodes. *J. Mater. Chem. A* **2023**, *11* (25), 13353−13370.
(53) Kok, D. J.; Irmscher, K.; Naumann, M.; Guguschev, C.; Galazka, Z.; Uecker, R. Temperature-Dependent Optical Absorption of $SrTiO_3$: Temperature-Dependent Optical Absorption of $SrTiO_3$. *Phys. Status Solidi A* **2015**, *212* (9), 1880−1887.
(54) Moos, R.; Härdtl, K. H. Dependence of the Intrinsic Conductivity Minimum of $SrTiO_3$ Ceramics on the Sintering Atmosphere. *J. Am. Ceram. Soc.* **1995**, *78* (9), 2569−2571.
(55) Jiang, W.; Noman, M.; Lu, Y. M.; Bain, J. A.; Salvador, P. A.; Skowronski, M. Mobility of Oxygen Vacancy in $SrTiO_3$ and Its Implications for Oxygen-Migration-Based Resistance Switching. *J. Appl. Phys.* **2011**, *110* (3), 034509.
(56) Abd Elkodous, M.; El-Khawaga, A. M.; Abouelela, M. M.; Abdel Maksoud, M. I. A. Cocatalyst Loaded Al-$SrTiO_3$ Cubes for Congo Red Dye Photo-Degradation under Wide Range of Light. *Sci. Rep.* **2023**, *13* (1), 6331.
(57) Muller, D. A.; Nakagawa, N.; Ohtomo, A.; Grazul, J. L.; Hwang, H. Y. Atomic-Scale Imaging of Nanoengineered Oxygen Vacancy Profiles in $SrTiO_3$. *Nature* **2004**, *430* (7000), 657−661.
(58) Cuong, D. D.; Lee, B.; Choi, K. M.; Ahn, H.-S.; Han, S.; Lee, J. Oxygen Vacancy Clustering and Electron Localization in Oxygen-Deficient $SrTiO_3$: LDA + U Study. *Phys. Rev. Lett.* **2007**, *98* (11), 115503.
(59) Kan, D.; Terashima, T.; Kanda, R.; Masuno, A.; Tanaka, K.; Chu, S.; Kan, H.; Ishizumi, A.; Kanemitsu, Y.; Shimakawa, Y.; Takano, M. Blue-Light Emission at Room Temperature from Ar^+-Irradiated $SrTiO_3$. *Nat. Mater.* **2005**, *4* (11), 816−819.
(60) Ohtomo, A.; Hwang, H. Y. Growth Mode Control of the Free Carrier Density in $SrTiO_{3-\delta}$ Films. *J. Appl. Phys.* **2007**, *102* (8), 083704.
(61) Hou, Z.; Terakura, K. Defect States Induced by Oxygen Vacancies in Cubic $SrTiO_3$: First-Principles Calculations. *J. Phys. Soc. Jpn.* **2010**, *79* (11), 114704.

https://doi.org/10.1021/jacs.5c07104
J. Am. Chem. Soc. XXXX, XXX, XXX−XXX

(62) Choi, M.; Oba, F.; Kumagai, Y.; Tanaka, I. Anti-Ferrodistortive-Like Oxygen-Octahedron Rotation Induced by the Oxygen Vacancy in Cubic $SrTiO_3$. *Adv. Mater.* **2013**, *25* (1), 86−90.
(63) Janotti, A.; Varley, J. B.; Choi, M.; Van de Walle, C. G. Vacancies and Small Polarons in $SrTiO_3$. *Phys. Rev. B* **2014**, *90* (8), 085202.
(64) Liu, B.; Cooper, V. R.; Xu, H.; Xiao, H.; Zhang, Y.; Weber, W. J. Composition Dependent Intrinsic Defect Structures in $SrTiO_3$. *Phys. Chem. Chem. Phys.* **2014**, *16* (29), 15590−15596.
(65) Moos, R.; Hardtl, K. H. Defect Chemistry of Donor-Doped and Undoped Strontium Titanate Ceramics between 1000° and 1400°C. *J. Am. Ceram. Soc.* **1997**, *80* (10), 2549−2562.
(66) Evarestov, R.; Blokhin, E.; Gryaznov, D.; Kotomin, E. A.; Merkle, R.; Maier, J. Jahn-Teller Effect in the Phonon Properties of Defective $SrTiO_3$ from First Principles. *Phys. Rev. B* **2012**, *85* (17), 174303.
(67) Ricca, C.; Timrov, I.; Cococcioni, M.; Marzari, N.; Aschauer, U. Self-Consistent DFT + U + V Study of Oxygen Vacancies in $SrTiO_3$. *Phys. Rev. Res.* **2020**, *2* (2), 023313.
(68) Wheeler, R. A.; Whangbo, M. H.; Hughbanks, T.; Hoffmann, R.; Burdett, J. K.; Albright, T. A. Symmetric vs. Asymmetric Linear M-X-M Linkages in Molecules, Polymers, and Extended Networks. *J. Am. Chem. Soc.* **1986**, *108* (9), 2222−2236.
(69) Lin, C.; Mitra, C.; Demkov, A. A. Orbital Ordering under Reduced Symmetry in Transition Metal Perovskites: Oxygen Vacancy in $SrTiO_3$. *Phys. Rev. B* **2012**, *86* (16), 161102.
(70) Mitra, C.; Lin, C.; Robertson, J.; Demkov, A. A. Electronic Structure of Oxygen Vacancies in $SrTiO_3$ and $LaAlO_3$. *Phys. Rev. B* **2012**, *86* (15), 155105.
(71) Lin, C.; Demkov, A. A. Electron Correlation in Oxygen Vacancy in $SrTiO_3$. *Phys. Rev. Lett.* **2013**, *111* (21), 217601.
(72) Kim, J.; Chung, C.-H.; Hong, K.-H. Understanding of the Formation of Shallow Level Defects from the Intrinsic Defects of Lead Tri-Halide Perovskites. *Phys. Chem. Chem. Phys.* **2016**, *18* (39), 27143−27147.
(73) Alkauskas, A.; Yan, Q.; Van De Walle, C. G. First-Principles Theory of Nonradiative Carrier Capture via Multiphonon Emission. *Phys. Rev. B* **2014**, *90* (7), 075202.
(74) Kim, S.; Márquez, J. A.; Unold, T.; Walsh, A. Upper Limit to the Photovoltaic Efficiency of Imperfect Crystals from First Principles. *Energy Environ. Sci.* **2020**, *13* (5), 1481−1491.
(75) Wang, X.; Kavanagh, S. R.; Scanlon, D. O.; Walsh, A. Upper Efficiency Limit of Sb_2Se_3 Solar Cells. *Joule* **2024**, *8*, P2105−2122.
(76) Turiansky, M. E.; Alkauskas, A.; Engel, M.; Kresse, G.; Wickramaratne, D.; Shen, J.-X.; Dreyer, C. E.; Van De Walle, C. G. Nonrad: Computing Nonradiative Capture Coefficients from First Principles. *Comput. Phys. Commun.* **2021**, *267*, 108056.
(77) Wilson, A. A.; Shalvey, T. P.; Kafizas, A.; Mumtaz, A.; Durrant, J. R. Analysis of Charge Trapping and Long Lived Hole Generation in $SrTiO_3$ Photoanodes. *Sustainable Energy Fuels* **2023**, *7* (20), 5066−5075.
(78) Fujisawa, J.; Eda, T.; Hanaya, M. Comparative Study of Conduction-Band and Valence-Band Edges of TiO_2, $SrTiO_3$, and $BaTiO_3$ by Ionization Potential Measurements. *Chem. Phys. Lett.* **2017**, *685*, 23−26.
(79) Kotani, T.; Ogawa, K.; Suzuki, H.; Kato, K.; Tomita, O.; Yamakata, A.; Abe, R. An Unexplored Role of the CrO_x Shell in an Elaborated Rh/CrO_x Core−Shell Cocatalyst for Photocatalytic Water Splitting: A Selective Electron Transport Pathway from Semiconductors to Core Metals, Boosting Charge Separation and H_2 Evolution. *EES Catal.* **2023**, *1* (3), 255−262.
(80) Rusevich, L. L.; Kotomin, E. A.; Zvejnieks, G.; Kržmanc, M. M.; Gupta, S.; Daneu, N.; Wu, J. C. S.; Lee, Y.-G.; Yu, W.-Y. Effects of Al Doping on Hydrogen Production Efficiency upon Photostimulated Water Splitting on $SrTiO_3$ Nanoparticles. *J. Phys. Chem. C* **2022**, *126*, 21223−21233.
(81) Krasikov, D.; Sankin, I. Defect Interactions and the Role of Complexes in the CdTe Solar Cell Absorber. *J. Mater. Chem. A* **2017**, *5* (7), 3503−3513.
(82) Wood, N. D.; Teter, D. M.; Tse, J. S.; Jackson, R. A.; Cooke, D. J.; Gillie, L. J.; Parker, S. C.; Molinari, M. An Atomistic Modelling Investigation of the Defect Chemistry of $SrTiO_3$ and Its Ruddlesden-Popper Phases, $Sr_{n+1}Ti_nO_{3n+1}$ (n = 1−3). *J. Solid State Chem.* **2021**, *303*, 122523.
(83) Blöchl, P. E. Projector Augmented-Wave Method. *Phys. Rev. B* **1994**, *50* (24), 17953−17979.
(84) Kresse, G.; Furthmüller, J. Efficient Iterative Schemes for *Ab Initio* Total-Energy Calculations Using a Plane-Wave Basis Set. *Phys. Rev. B* **1996**, *54* (16), 11169−11186.
(85) Kresse, G.; Joubert, D. From Ultrasoft Pseudopotentials to the Projector Augmented-Wave Method. *Phys. Rev. B* **1999**, *59* (3), 1758−1775.
(86) Paier, J.; Marsman, M.; Hummer, K.; Kresse, G.; Gerber, I. C.; Ángyán, J. G. Screened Hybrid Density Functionals Applied to Solids. *J. Chem. Phys.* **2006**, *124* (15), 154709.
(87) Li, K.; Willis, J.; Kavanagh, S.R.; Scanlon, D.O. Computational Prediction of an Antimony-Based n-Type Transparent Conducting Oxide: F-Doped Sb2O5. *Chem. mater* **2024**, *36*, 2907−2916.
(88) Gajdoš, M.; Hummer, K.; Kresse, G.; Furthmüller, J.; Bechstedt, F. Linear Optical Properties in the Projector-Augmented Wave Methodology. *Phys. Rev. B* **2006**, *73* (4), 045112.
(89) Perdew, J. P.; Burke, K.; Ernzerhof, M. Generalized Gradient Approximation Made Simple. *Phys. Rev. Lett.* **1996**, *77* (18), 3865−3868.
(90) Ganose, M.; A, J. J.; A, O. S. D. Sumo: Command-Line Tools for Plotting and Analysis of Periodic Ab Initio Calculations. *JOSS* **2018**, *3* (28), 717.
(91) Dronskowski, R.; Bloechl, P. E. Crystal Orbital Hamilton Populations (COHP): Energy-Resolved Visualization of Chemical Bonding in Solids Based on Density-Functional Calculations. *J. Phys. Chem.* **1993**, *97* (33), 8617−8624.
(92) Zhao, X.-G.; Wang, Z.; Malyi, O. I.; Zunger, A. Effect of Static Local Distortions vs. Dynamic Motions on the Stability and Band Gaps of Cubic Oxide and Halide Perovskites. *Materials Today* **2021**, *49*, 107−122.
(93) Kasamatsu, S.; Tada, T.; Watanabe, S. Theoretical Analysis of Space Charge Layer Formation at Metal/Ionic Conductor Interfaces. *Solid State Ionics.* **2011**, *183* (1), 20−25.
(94) Neilson, W. D.; Murphy, S. T. DefAP: A Python Code for the Analysis of Point Defects in Crystalline Solids. *Comput. Mater. Sci.* **2022**, *210*, 111434.
(95) Kavanagh, S. R.; Scanlon, D. O.; Walsh, A.; Freysoldt, C. Impact of Metastable Defect Structures on Carrier Recombination in Solar Cells. *Faraday Discuss.* **2022**, *239*, 339−356.
(96) Mosquera-Lois, I.; Kavanagh, S. R.; Klarbring, J.; Tolborg, K.; Walsh, A. Imperfections Are Not 0 K: Free Energy of Point Defects in Crystals. *Chem. Soc. Rev.* **2023**, *52* (17), 5812−5826.
(97) Wang, V.; Xu, N.; Liu, J.-C.; Tang, G.; Geng, W.-T. VASPKIT: A User-Friendly Interface Facilitating High-Throughput Computing and Analysis Using VASP Code. *Comput. Phys. Commun* **2021**, *267*, 108033.
(98) Kim, S.; Hood, S.; Van Gerwen, P.; Whalley, L.; Walsh, A. CarrierCapture.Jl: Anharmonic Carrier Capture. *JOSS* **2020**, *5* (47), 2102.
(99) Pässler, R. Relationships between the Nonradiative Multi-phonon Carrier-capture Properties of Deep Charged and Neutral Centres in Semiconductors. *Phys. Status Solidi B* **1976**, *78* (2), 625−635.

https://doi.org/10.1021/jacs.5c07104
J. Am. Chem. Soc. XXXX, XXX, XXX−XXX